19th AIAA Computational Fluid Dynamics
22 - 25 June 2009, San Antonio, Texas

AIAA 2009-3784

A High-order Lifting Collocation Penalty Formulation for the Navier-Stokes Equations on 2D Mixed Grids

Haiyang Gao[1] and Z.J. Wang[2]
Department of Aerospace Engineering and CFD Center, Iowa State University, Ames, IA, 50011

The newly developed lifting collocation penalty (LCP) formulation for conservation laws is extended to solve the Navier-Stokes equations on 2D mixed meshes. The LCP formulation is an extension of the flux reconstruction (FR) method. Like the FR method, it can unify several popular high order methods including the discontinuous Galerkin and the spectral volume methods into a more efficient differential form. For the discretization of viscous fluxes, two compact formulations are employed, including the 2nd approach of Bassi and Rebay (BR2) and the I-continuous approach recently introduced by Huynh (2009). Several test cases are conducted with the implicit LU-SGS scheme to demonstrate the capability of the LCP formulation.

I. Introduction

While 2nd order methods are dominant in most compressible flow simulations on unstructured meshes, many types of problems, such as computational aeroacoustics, vortex-dominant flows and large eddy simulation (LES) of turbulent flows, call for higher order accuracy. Various high order methods have been developed in the last two decades, including the discontinuous Galerkin (DG) method [1-5], the spectral volume (SV) method [6-10], and the spectral difference (SD) method [11-13]. The above-mentioned methods have a common feature: they achieve high order accuracy by locally approximating the solutions as a high order polynomial inside a cell or element. Therefore the solution space is piecewise discontinuous polynomials of degree k, with a (k+1)th order of accuracy. The difference between these methods lies in the definition of degrees of freedom (DOFs) and how the DOFs are updated.

Huynh (2007) [14] unified all the above methods in 1D with the introduction of the flux reconstruction (FR) method. Wang and Gao (2009) [15] extended the idea to 2D triangular and mixed meshes with the lifting collocation penalty (LCP) formulation, and applied this formulation to solve the 2D Euler equations. The LCP formulation resulted in a highly efficient differential scheme without involving numerical integrations for almost arbitrary meshes. The present study aims at further extending the formulation for the solution of the Navier-Stokes equations. The central issue of this study is the discretization of the viscous terms in the LCP formulation.

Numerous studies have been performed for the treatment of the diffusion terms in high order methods. The first [5] and second [16] approaches of Bassi and Rebay (BR1 and BR2) are the first successful ones solving the Navier-Stokes equations. However, although the BR2 approach is compact, the BR1 approach is not. Later the LDG approach [17] was developed to address the disretization of viscous terms. The LDG approach demonstrated uniform accuracy, but the approach is not compact on general unstructured meshes. The non-compact property was remedied with the developed of the compact DG (CDG) approach [18]. Van Leer and Nomura [19] developed a very accurate recovery approach for the DG method, but it is more expensive computationally than the other approaches in multiple dimensions, because a reconstruction across two adjacent cells is needed for each interface. Huynh (2009) [20] unified several approaches into the FR formulation, and also proposed the I-continuous approach based on a continuous local reconstruction at each interface.

If the residual of the DOFs inside one cell is only dependent on the solution of this cell and its face neighbors, the spatial scheme is said to be compact. Being compact is a highly desirable property for implicit time integration and for parallel computing. Therefore in the present study, two compact approaches for viscous terms– the BR2 and I-continuous approaches - are adapted to the LCP formulation.

Hybrid meshes provide the most flexibility in handling a complex geometry. In addition, they are also more suitable in tackling viscous boundary layers. Liang et al [21] developed an SD solver for the N-S equations on

[1] Graduate Research Assistant, Department of Aerospace Engineering, 2271 Howe Hall, AIAA Member.
[2] Professor of Aerospace Engineering, 2271 Howe Hall, Associate Fellow of AIAA.

mixed meshes. Their approach was to perform a one-level h-refinement to convert a mixed mesh to a finer quadrilateral mesh. In the present study, however, triangular and quadrilateral cells are treated separately, and their interfaces are connected by the same distribution of flux points to maximize efficiency, as shown in Figure 1.

The paper is organized as follows: Section 2 reviews the FR and LCP formulations for mixed meshes and describes the discretization of viscous terms; Section 3 presents numerical tests with the Couette flow, the flow around a NACA 0012 airfoil and the flow around a circular cylinder; several conclusions are drawn in Section 4.

II. Numerical Formulations

2.1 Governing Equations

The 2D Navier-Stokes equations can be written in the following conservation form:

$$\frac{\partial Q}{\partial t}+\frac{\partial F}{\partial x}+\frac{\partial G}{\partial y}=0 \tag{2.1}$$

where Q is the vector of conserved variable, and F and G include both the inviscid and viscous flux vectors, i.e., $F=F^i-F^v, G=G^i-G^v$, which take the following form

$$Q=\begin{Bmatrix}\rho\\ \rho u\\ \rho v\\ E\end{Bmatrix}, F^i=\begin{Bmatrix}\rho u\\ p+\rho u^2\\ \rho uv\\ u(E+p)\end{Bmatrix}, G^i=\begin{Bmatrix}\rho v\\ \rho uv\\ p+\rho v^2\\ v(E+p)\end{Bmatrix}, \tag{2.2}$$

and

$$F^v=\mu\begin{Bmatrix}0\\ 2u_x+\lambda(u_x+v_y)\\ v_x+u_y\\ u\left[2u_x+\lambda(u_x+v_y)\right]+v(v_x+u_y)+\dfrac{C_p}{\mathrm{Pr}}T_x\end{Bmatrix}, \tag{2.3}$$

$$G^v=\mu\begin{Bmatrix}0\\ v_x+u_y\\ 2v_y+\lambda(u_x+v_y)\\ u(v_x+u_y)+v\left[2v_y+\lambda(u_x+v_y)\right]+\dfrac{C_p}{\mathrm{Pr}}T_y\end{Bmatrix}.$$

In (2.1)-(2.3), ρ is the density, u and v are velocity components in x and y directions, p is the pressure, and E is the total energy, μ is the dynamic viscosity, C_p is the specific heat at constant pressure, Pr is the Prandle number, and T is the temperature. For a perfect gas, the pressure is related to the total energy by

$$E=\frac{p}{\gamma-1}+\frac{1}{2}\rho(u^2+v^2)\cdot \tag{2.4}$$

The ratio of specific heats γ is assumed to be a constant, 1.4 for air. λ is set to *-2/3* according to the Stokes hypothesis.

2.2 Review of the Flux Reconstruction (FR) Method

This review presents the essential idea of the flux reconstruction developed by Huynh [14]. This method is extended to 2D quadrilateral cells with a tensor product approach.

2.2.1 1D FR Method

Consider the following scalar conservation law

$$\frac{\partial Q}{\partial t}+\frac{\partial F(Q)}{\partial x}=0\,, \tag{2.5}$$

where Q is the state variable and F is the flux. The computational domain *[a, b]* is discretized into N elements, with the *ith* element defined by $V_i \equiv [x_{i-1/2}, x_{i+1/2}]$. Each element can be transformed into the standard element *[-1, 1]* using a linear transformation. The DOFs at the *ith* element are the nodal values of the state variable $Q_{i,j}$ at $k+1$ solution points, $x_{i,j}$, $j = 1, ..., k+1$. Then the solution is approximated by the following degree k Lagrange interpolation polynomial

$$Q(x)\approx Q_i^h(x)=\sum_{j=1}^{k+1}L_j(x)Q_{i,j}\,, \tag{2.6}$$

where $L_j(x)$ is the Lagrange polynomial or shape function. Given this numerical solution, the flux at every point is well defined, i.e., $F(Q_i^h(x))$. For non-linear conservation laws, $F(Q_i^h(x))$ may not be a polynomial. Instead, $F(Q_i^h(x))$ is approximated by the following degree k flux polynomial

$$F_i\ (x)=\sum_{j=1}^{k+1}L_j(x)F(Q_i^h(x_{i,j}))\cdot \tag{2.7}$$

Since we do not explicitly enforce continuity at element interfaces, the state variable is discontinuous across the interfaces. In order to update the DOFs, a new flux function $\hat{F}_i(x)$ is reconstructed, which must satisfy the following criteria:

- $\hat{F}_i(x)$ is a degree $k+1$ polynomial, i.e., one degree higher than the solution polynomial;
- $\hat{F}_i(x)$ is close to $F_i\ (x)$ in some sense. In other words, some norm of the difference $\left\|\hat{F}_i(x)-F_i\ (x)\right\|$ is minimized;
- At both ends of the element, the flux takes on the value of the Riemann fluxes, i.e.,

$$\hat{F}_i(x_{i-1/2})=\tilde{F}(Q_{i-1}(x_{i-1/2}),Q_i(x_{i-1/2}))\equiv\tilde{F}_{i-1/2}$$

$$\hat{F}_i(x_{i+1/2})=\tilde{F}(Q_i(x_{i+1/2}),Q_{i+1}(x_{i+1/2}))\equiv\tilde{F}_{i+1/2}\,,$$

where $\tilde{F}(Q^-,Q^+)$ is a well-defined common face flux given the two discontinuous solutions at the left and right of the interface (such as any Riemann flux for inviscid flow). Once this flux function is found, the DOFs are updated using the following differential equation

$$\frac{\partial Q_{i,j}}{\partial t}+\frac{\partial \hat{F}_i(x_{i,j})}{\partial x}=0\,. \tag{2.8}$$

Obviously the above criteria do not uniquely define $\hat{F}_i(x)$, since only the two end conditions are prescribed. The reconstructed flux is first re-written as

$$\hat{F}_i(x)=F_i\ (x)+\sigma_i(x)\,, \tag{2.9}$$

where $\sigma_i(x)$ is a correction flux polynomial, which should be as close as possible to 0. The correction is then further expressed to satisfy the two end conditions

$$\sigma_i(x) = [\tilde{F}_{i-1/2} - F_i\ (x_{i-1/2})]g_L(x) + [\tilde{F}_{i+1/2} - F_i\ (x_{i+1/2})]g_R(x), \tag{2.10}$$

where $g_L(x)$ and $g_R(x)$ are both degree $k+1$ polynomials called correction functions, and they satisfy

$$\begin{aligned} g_L(x_{i-1/2}) &= 1, \quad g_L(x_{i+1/2}) = 0 \\ g_R(x_{i-1/2}) &= 0, \quad g_R(x_{i+1/2}) = 1. \end{aligned} \tag{2.11}$$

Eq. (2.8) then becomes

$$\frac{\partial Q_{i,j}}{\partial t} + \frac{\partial F_i\ (x_{i,j})}{\partial x} + [\tilde{F}_{i-1/2} - F_i\ (x_{i-1/2})]g_L'(x_{i,j}) + [\tilde{F}_{i+1/2} - F_i\ (x_{i+1/2})]g_R'(x_{i,j}) = 0\,. \tag{2.12}$$

Because of symmetry, we only need to consider $g_L(x)$, or simply $g(x)$. It is more convenient to consider the correction function in the standard element $g(\xi)$ on [-1, 1]. Using special polynomials such as the Radau and Legendre polynomials, Huynh [14] successfully recovered $\hat{F}_i(x)$ for the DG, staggered grid (SG) [22] (or SD/SV) methods, at least for linear conservations laws. In the present study, only the correction corresponding to the DG method is used.

2.2.2 2D FR Method for Quadrilateral Cells

It is very straight-forward to extend the FR method to quadrilateral cells, first any arbitrary quadrilateral cell is transformed to a standard square element $(\xi,\eta) \in$[-1,1]x[-1,1] as shown in Figure 2. The transformation can be written as

$$\begin{pmatrix} x \\ y \end{pmatrix} = \sum_{i=1}^{K} M_i(\xi,\eta) \begin{pmatrix} x_i \\ y_i \end{pmatrix}, \tag{2.13}$$

where K is the number of points used to define the physical element, (x_i, y_i) are the Cartesian coordinates of those points, and $M_i(\xi,\eta)$ are the shape functions. For the transformation given in Eq. (2.13), the Jacobian matrix J takes the following form

$$J = \frac{\partial(x,y)}{\partial(\xi,\eta)} = \begin{bmatrix} x_\xi & x_\eta \\ y_\xi & y_\eta \end{bmatrix}. \tag{2.14}$$

For a non-singular transformation, its inverse transformation must also exist, and the Jacobian matrices are related to each other according to

$$\frac{\partial(\xi,\eta)}{\partial(x,y)} = \begin{bmatrix} \xi_x & \xi_y \\ \eta_x & \eta_y \end{bmatrix} = J^{-1}.$$

Therefore the metrics can be computed according to

$$\xi_x = y_\eta/|J|, \quad \xi_y = -x_\eta/|J|, \quad \eta_x = -y_\xi/|J|, \quad \eta_y = x_\xi/|J|. \tag{2.15}$$

The governing equations in the physical domain are then transformed into the computational domain (standard element), and the transformed equations take the following form

$$\frac{\partial \tilde{Q}}{\partial t} + \frac{\partial F^\xi}{\partial \xi} + \frac{\partial F^\eta}{\partial \eta} = 0\,. \tag{2.16}$$

where

$$\tilde{Q} = |J| \cdot Q \tag{2.17}$$

$$F^{\xi} = |J|(\xi_x F^x + \xi_y F^y) \tag{2.18}$$

$$F^{\eta} = |J|(\eta_x F^x + \eta_y F^y). \tag{2.19}$$

Let $\vec{S}_{\xi} = |J|(\xi_x, \xi_y)$, $\vec{S}_{\eta} = |J|(\eta_x, \eta_y)$. Then we have $F^{\xi} = \vec{F} \bullet \vec{S}_{\xi}, F^{\eta} = \vec{F} \bullet \vec{S}_{\eta}$. In our implementation, $|J|$ and $\vec{S}_{\xi}$, $\vec{S}_{\eta}$ are stored at the solution points. Within the *ith* element, the solution polynomial is a tensor product of 1D Lagrange polynomials, i.e.,

$$Q_i^h(\xi, \eta) = \sum_{l=1}^{k+1} \sum_{j=1}^{k+1} Q_{i;j,l}^h L_j(\xi) \cdot L_l(\eta), \tag{2.20}$$

where $Q_{i;j,l}^h$ are the state variables at the solution point (*j*,*l*), with *j* the index in ξ direction and *l* the index in η direction, $L_j(\xi)$ and $L_l(\eta)$ are 1D Lagrange polynomials in ξ and η directions. Based on the reconstructed solution $Q_i^h(\xi, \eta)$, the fluxes can be defined using $F^{\xi}(Q_i^h), F^{\eta}(Q_i^h)$. Again, one can also choose to represent the fluxes with Lagrange interpolation polynomials in the following form:

$$F_i^{\xi}(\xi, \eta) = \sum_{l=1}^{k+1} \sum_{j=1}^{k+1} F_{i;j,l}^{\xi} L_j(\xi) \cdot L_l(\eta), \tag{2.21a}$$

$$F_i^{\eta}(\xi, \eta) = \sum_{l=1}^{k+1} \sum_{j=1}^{k+1} F_{i;j,l}^{\eta} L_j(\xi) \cdot L_l(\eta) \cdot \tag{2.21b}$$

Again common face fluxes are computed at all four element interfaces in the normal directions, which are the same or opposite directions of $\vec{S}_{\xi}$ or $\vec{S}_{\eta}$.

Therefore the Riemann flux corresponding to F^{ξ} is computed according to

$$\tilde{F}^{\xi}(-1, \eta) = -\tilde{F}^n(Q_i(-1, \eta), Q_{i+}(-1, \eta), \vec{n})|\vec{S}_{\xi}|, \tag{2.22a}$$

$$\tilde{F}^{\xi}(1, \eta) = \tilde{F}^n(Q_i(1, \eta), Q_{i+}(1, \eta), \vec{n})|\vec{S}_{\xi}|. \tag{2.22b}$$

Finally the DOFs are updated using the following equation

$$\begin{aligned} &\frac{\partial \tilde{Q}_{i;j,l}}{\partial t} + \frac{\partial F_i^{\xi}(\xi_{j,l}, \eta_{j,l})}{\partial \xi} + \frac{\partial F_i^{\eta}(\xi_{j,l}, \eta_{j,l})}{\partial \eta} \\ &+ [\tilde{F}^{\xi}(-1, \eta_{j,l}) - F_i^{\xi}(-1, \eta_{j,l})] g_L'(\xi_{j,l}) + [\tilde{F}^{\xi}(1, \eta_{j,l}) - F_i^{\xi}(1, \eta_{j,l})] g_R'(\xi_{j,l}) \\ &+ [\tilde{F}^{\eta}(\xi_{j,l}, -1) - F_i^{\eta}(\xi_{j,l}, -1)] g_L'(\eta_{j,l}) + [\tilde{F}^{\eta}(\xi_{j,l}, 1) - F_i^{\eta}(\xi_{j,l}, 1)] g_R'(\eta_{j,l}) = 0. \end{aligned} \tag{2.23}$$

Note that the correction is done in a "one dimensional" manner, thus the 1D approach can be followed.

2.3 Review of the LCP Formulation for Conservation Laws

For more general 2D elements like triangular ones, a direct implementation of the FR method is quite involved. The LCP formulation is developed for this purpose, with exceptionally good properties for triangular elements. Let's express the hyperbolic conservation law as

$$\frac{\partial Q}{\partial t} + \nabla \bullet \vec{F}(Q) = 0, \tag{2.24}$$

where $\vec{F} = (F, G)$ is the flux vector. The computational domain is discretized into *N* non-overlapping elements $\{V_i\}$. Let *W* be an arbitrary weighting function. The weighted residual form of Eq. (2.24) on element V_i can be easily derived by multiplying Eq. (2.24) with *W* and integrating over V_i to obtain

$$\int_{V_i} \left(\frac{\partial Q}{\partial t} + \nabla \bullet \vec{F}(Q) \right) W dV = \int_{V_i} \frac{\partial Q}{\partial t} W dV + \int_{\partial V_i} W \vec{F}(Q) \bullet \vec{n} dS - \int_{V_i} \nabla W \bullet \vec{F}(Q) dV = 0. \tag{2.25}$$

Let Q_i^h be an approximate solution to *Q* at element *i*. We assume that the solution belongs to the space of polynomials of degree *k* or less, i.e., $Q_i^h \in P^k$, within each element without continuity requirement across element interfaces. In addition, the numerical solution Q_i^h must also satisfy Eq. (2.25), i.e.,

$$\int_{V_i} \frac{\partial Q_i^h}{\partial t} W dV + \int_{\partial V_i} W \vec{F}(Q_i^h) \bullet \vec{n} dS - \int_{V_i} \nabla W \bullet \vec{F}(Q_i^h) dV = 0. \tag{2.26}$$

Since the solution is discontinuous across element interfaces, the surface integral in Eq. (2.26) is not well-defined. To remedy this problem, a common flux is used to replace the normal flux to provide element coupling, i.e.,

$$F^n(Q_i^h) \equiv \vec{F}(Q_i^h) \bullet \vec{n} \approx \tilde{F}^n(Q_i^h, Q_{i+}^h, \vec{n}), \tag{2.27}$$

where Q_{i+}^h is the solution outside the current element V_i. Then Eq. (2.26) becomes

$$\int_{V_i} \frac{\partial Q_i^h}{\partial t} W dV + \int_{\partial V_i} W \tilde{F}^n(Q_i^h, Q_{i+}^h, \vec{n}) dS - \int_{V_i} \nabla W \bullet \vec{F}(Q_i^h) dV = 0. \tag{2.28}$$

Applying integration by parts to the last term on the LHS of Eq. (2.28), we obtain

$$\int_{V_i} \frac{\partial Q_i^h}{\partial t} W dV + \int_{V_i} W \nabla \bullet \vec{F}(Q_i^h) dV + \int_{\partial V_i} W \left[\tilde{F}^n(Q_i^h, Q_{i+}^h, \vec{n}) - F^n(Q_i^h) \right] dS = 0. \tag{2.29}$$

The last term in Eq. (2.29) can be viewed as a penalty term, i.e., penalizing the normal flux differences. Introduce a "correction field" $\delta_i \in P^k$, which is determined from a "lifting operator"

$$\int_{V_i} W \delta_i dV = \int_{\partial V_i} W [\tilde{F}] dS, \tag{2.30}$$

where $[\tilde{F}] = \tilde{F}^n(Q^h, Q^{h+}, \vec{n}) - F^n(Q^h)$ is the normal flux difference. Substituting Eq. (2.30) into Eq. (2.29), we obtain

$$\int_{V_i} \left[\frac{\partial Q_i^h}{\partial t} + \nabla \bullet \vec{F}(Q_i^h) + \delta_i \right] W dV = 0. \tag{2.31}$$

Because W is arbitrary, Eq. (2.31) is equivalent to

$$\frac{\partial Q_i^h}{\partial t} + \nabla \bullet \vec{F}(Q_i^h) + \delta_i = 0, \tag{2.32}$$

i.e., Eq. (2.32) is satisfied everywhere in element V_i. With the definition of a correction field δ_i, we have successfully reduced the weighted residual formulation to an equivalent simple differential form, which does not involve any explicit surface or volume integrals. The lifting operator obviously depends on the choice of weighting function. If $W \in P^k$, Eq. (2.32) is equivalent to the DG formulation.

Next let the degrees-of-freedom (DOFs) be the solutions at a set of points $\{\vec{r}_{i,j}\}$, named solution points (SPs), as shown in Figure 3. Then Eq. (2.32) must be true at the SPs, i.e.,

$$\frac{\partial Q_{i,j}^h}{\partial t} + \nabla \bullet \vec{F}(Q_{i,j}^h) + \delta_{i,j} = 0, \tag{2.33}$$

where $\nabla \bullet \vec{F}(Q_{i,j}^h) = \left[\nabla \bullet \vec{F}(Q^h)\right]_{\vec{r}_{i,j}}$. And for a specific set of solution points and flux points, the correction at SPs can be derived to take the following form.

$$\delta_{i,j} = \frac{1}{|V_i|} \sum_{f \in \partial V_i} \sum_l \alpha_{j,f,l} [\tilde{F}]_{f,l} S_f, \tag{2.34}$$

where $\alpha_{j,f,l}$ are constant scheme coefficients independent of the solution, or the shape of the triangle, but dependent on the location of solution points and the test functions chosen. Especially Substituting (2.33) into (2.34) we obtain the following LCP formulation

$$\frac{\partial Q_{i,j}^h}{\partial t} + \nabla \bullet \vec{F}(Q_{i,j}^h) + \frac{1}{|V_i|} \sum_{f \in \partial V_i} \sum_l \alpha_{j,f,l} [\tilde{F}]_{f,l} S_f = 0 \cdot \tag{2.35}$$

It can be shown that the location of SPs does not affect the numerical scheme for linear conservation laws. For efficiency, the solution points are always chosen to coincide with the flux points. For 2D faces (or edges), the flux points are the Legendre Lobatto points for both triangular and quadrilateral cells to minimize the complexity of the interface treatment.

2.4 Inviscid Flux Discretization

With the formulations for quadrilateral and triangular elements defined in Section 2.2 and 2.3, we still need to discretize the numerical flux. This includes two parts: find the internal flux divergence $\nabla \bullet \vec{F}$; evaluate the common flux at the interface. Let's first start with the inviscid terms.

Instead of approximating the inviscid flux by a Lagrange polynomial, the flux divergence is computed "exactly" by a chain rule (CR) approach

$$\nabla \bullet \vec{F}(Q_i^h) = \frac{\partial F^x(Q_i^h)}{\partial x} + \frac{\partial F^y(Q_i^h)}{\partial y} = \frac{\partial F^x}{\partial Q}\frac{\partial Q_i^h}{\partial x} + \frac{\partial F^y}{\partial Q}\frac{\partial Q_i^h}{\partial y} = \frac{\partial \vec{F}}{\partial Q} \bullet \nabla Q_i^h \tag{2.36}$$

The common inviscid flux at the interfaces can be obtained with any Riemann solver. In the present study, Roe flux [23] is used for all the cases presented later.

2.5 Viscous Flux Discretization

2.5.1 Basic Framework

The viscous fluxes $F^v(Q,\nabla Q)$ and $G^v(Q,\nabla Q)$ are functions of both the conserved variables and their gradients. In order to compute the divergence of the viscous flux, we follow the formulation in [5] by introducing a new variable R:

$$R = \nabla Q \Rightarrow R - \nabla Q = 0 \tag{2.37}$$

Eq. (2.37) is solved in the weak DG formulation, and in our LCP framework, this will result in a collocation formulation

$$R_{i,j} = \left(\nabla Q_i^h\right)_j + \frac{1}{|V_i|}\sum_{f\in\partial V_i}\sum_l \alpha_{j,f,l}[\tilde{Q}]_{f,l}\vec{n}_f S_f \tag{2.38}$$

where $[\tilde{Q}]_{f,l} = Q_{f,l}^{com} - Q_{i;f,l}$, $Q_{f,l}^{com}$ is the common solution on interface *f*, and $Q_{i;f,l}$ is the solution within cell *i* on face *f*. The definition of $Q^{com} = Q^{com}\left(Q^+, Q^-, \vec{n}\right)$ varies with different approaches to discretize the viscous terms. Note that Eq. (2.38) is for triangular elements. A similar formulation for 1D or quadrilateral element is straight-forward to derive.

After this, the viscous fluxes at solution points are evaluated by

$$F_{i,j}^v = F^v\left(Q_{i,j}, R_{i,j}\right), G_{i,j}^v = G^v\left(Q_{i,j}, R_{i,j}\right). \tag{2.39}$$

And with the fluxes at solution points, $\frac{\partial F^v}{\partial x}$ and $\frac{\partial G^v}{\partial y}$ can be easily obtained through Lagrange reconstruction.

Besides those interior derivatives, common viscous fluxes at the interfaces are also needed for the LCP formulation

$$F_{f,l}^{com} = F^v\left(Q_{f,l}^{com}, \nabla Q_{f,l}^{com}\right), G_{f,l}^{com} = G^v\left(Q_{f,l}^{com}, \nabla Q_{f,l}^{com}\right) \tag{2.40}$$

This means we also need to define a common gradient $\nabla Q^{com} = \nabla Q^{com}\left(\nabla Q^+, \nabla Q^-, Q^+, Q^-, \vec{n}\right)$ on the cell interfaces. The definition also depends on the approach to discretize the viscous terms.

In the following sections, the ways to define Q^{com} and ∇Q^{com} in both the BR2 and I-continuous approaches are described.

2.5.2 BR2

The common solution in BR2 is simply the average of solutions at two sides of the face

$$Q_{f,l}^{com} = \frac{Q_{f,l}^- + Q_{f,l}^+}{2}. \tag{2.41}$$

For the common gradient, the definition can be written as

$$\nabla Q_{f,l}^{com} = \frac{1}{2}\left(\nabla Q_{f,l}^- + r_{f,l}^- + \nabla Q_{f,l}^+ + r_{f,l}^+\right). \tag{2.42}$$

where $\nabla Q_{f,l}^-$ and $\nabla Q_{f,l}^+$ are the gradients of the solution of the left and right cells, while $r_{f,l}^-$ and $r_{f,l}^+$ are the corrections to the gradients only due to the common the solution on face *f*

$$r_{f,l}^- = \frac{1}{|V^-|}\sum_m \beta_{f,l,m}[\tilde{Q}]_{f,m}^- \vec{n}_f S_f, \quad r_{f,l}^+ = \frac{1}{|V^+|}\sum_m \beta_{f,l,m}[\tilde{Q}]_{f,m}^+ \left(-\vec{n}_f\right) S_f \tag{2.43a}$$

Eq. (2.43a) is used for triangular cells, where $[\tilde{Q}]_{f,l}^{-}=Q_{f,l}^{com}-Q_{f,l}^{-}$,$[\tilde{Q}]_{f,l}^{+}=Q_{f,l}^{com}-Q_{f,l}^{+}$, $\beta_{f,l,m}$ is the coefficient of correction due to face *f*. $\beta_{f,l,m}$ can be extracted from coefficients $\alpha_{j,f,l}$ in Eq. (2.34), and due to the symmetry of triangles, $\beta_{f,l,m}$ for any face *f* is identical for a fixed distribution of flux points, thus the face index is omitted from here on.

For quadrilateral elements, we have similar equations in FR formulation

$$r_{f,l}^{-}=-[\tilde{Q}]_{f,l}^{-}g'(-1)\left(\xi_x,\xi_y\right)^{-},\quad r_{f,l}^{+}=[\tilde{Q}]_{f,l}^{+}g'(-1)\left(\xi_x,\xi_y\right)^{+}. \tag{2.43b}$$

$g'(-1)$ in Eq. (2.43b) serves as a coefficient to penalize the solution difference on different sides of the face. In the actual implementation, it is discovered that if we use $g_{DG}'(-1)$, i.e. the derivative of the Radau polynomial (the value is $-K^2/2$ for degree *K* polynomial), the resulted scheme is unstable for N-S equations. Therefore, a slightly bigger coefficient $-(K+1)(K+2)/2$ is used in simulations presented later.

2.5.3 I-continuous

The I-continuous approach in 1D was proposed in Huynh (2009) [20]. Its basic idea is: instead of prescribing a common solution Q^{com} at the interfaces, Q^{com} is solved so that the corrected derivative $\frac{\partial Q^{C}}{\partial x}$ is continuous at the interface. In this way, the common derivative $\frac{\partial Q^{com}}{\partial x}$ is also well-defined, since there is only one value at the interface.

However, in 2D cases, requiring ∇Q^{C} to be continuous at the interfaces gives us two conditions –continuity in *x* and *y* directions. Since we are only solving one variable Q^{com}, we only require the continuity in the face normal direction. If both sides of the face are quadrilateral elements, the corrected gradients can be written as

$$\nabla Q_{f,l}^{C-}=\nabla Q_{f,l}^{-}-[\tilde{Q}]_{f,l}^{-}g'(1)\left(\xi_x,\xi_y\right)^{-},\nabla Q_{f,l}^{C+}=\nabla Q_{f,l}^{+}+[\tilde{Q}]_{f,l}^{+}g'(1)\left(\xi_x,\xi_y\right)^{+}. \tag{2.44}$$

Then we require the gradient to be continuous in the normal direction

$$\nabla Q^{C-}\cdot\vec{n}=\nabla Q^{C+}\cdot\vec{n}\,. \tag{2.45}$$

Substituting in (2.44), we have

$$\nabla Q_{f,l}^{-}\cdot\vec{n}-\left(Q_{f,l}^{com}-Q_{f,l}^{-}\right)g'(-1)\left(\sqrt{\xi_x^2+\xi_y^2}\right)^{-}=\nabla Q_{f,l}^{+}\cdot\vec{n}+\left(Q_{f,l}^{com}-Q_{f,l}^{+}\right)g'(-1)\left(\sqrt{\xi_x^2+\xi_y^2}\right)^{+}. \tag{2.46}$$

The only unknown in (2.46) is $Q_{f,l}^{com}$, after $Q_{f,l}^{com}$ is solved from (2.46), the common viscous flux at the interface can be obtained by

$$\begin{aligned}&\nabla Q_{f,l}^{com}\cdot\vec{n}=\nabla Q^{C-}\cdot\vec{n}\qquad or\qquad \nabla Q_{f,l}^{com}\cdot\vec{n}=\nabla Q^{C+}\cdot\vec{n}\\&\nabla Q_{f,l}^{com}\cdot\vec{t}=\frac{\nabla Q_{f,l}^{-}\cdot\vec{t}+\nabla Q_{f,l}^{+}\cdot\vec{t}}{2}\end{aligned} \tag{2.47}$$

If both sides of the face are triangular cells, the corrected gradients is

$$\nabla Q_{f,l}^{C-}=\nabla Q_{f,l}^{-}+\frac{S_f}{\left|V^{-}\right|}\sum_m[\tilde{Q}]_{f,m}^{-}\beta_{l,m}\vec{n},\quad \nabla Q_{f,l}^{C+}=\nabla Q_{f,l}^{+}+\frac{S_f}{\left|V^{+}\right|}\sum_m[\tilde{Q}]_{f,m}^{+}\beta_{l,m}\left(-\vec{n}\right) \tag{2.48}$$

Substituting into (2.45), after some derivation,

$$S_f\left(\frac{1}{|V^-|}+\frac{1}{|V^+|}\right)\sum_m \beta_{l,m}Q^{com}_{f,m}=\nabla Q^+_{f,l}\cdot\vec{n}-\nabla Q^-_{f,l}\cdot\vec{n}+S_f\sum_m\beta_{l,m}\left(\frac{Q^-_{f,m}}{|V^-|}+\frac{Q^+_{f,m}}{|V^+|}\right) \tag{2.49}$$

Eq. (2.49) represents a linear system, from which $Q^{com}_{f,l}$ can be easily solved. Then, the common viscous flux ∇Q^{com} is obtained through (2.47).

For a mixed mesh, there is another situation, when the face has a quadrilateral cell on one side and a triangular cell on the other side. Without the loss of generality, assume the left (-) cell to be triangular, then the corrected gradients are

$$\nabla Q^{C-}_{f,l}=\nabla Q^-_{f,l}+\frac{S_f}{|V^-|}\sum_m[\tilde{Q}]^-_{f,m}\beta_{l,m}\vec{n},\nabla Q^{C+}_{f,l}=\nabla Q^+_{f,l}+[\tilde{Q}]^+_{f,l}g'(1)\left(\xi_x,\xi_y\right)^+\cdot \tag{2.50}$$

Again this is substituted into (2.45), we can derive

$$\begin{aligned}&\frac{S_f}{|V^-|}\sum_m\beta_{l,m}Q^{com}_{f,m}-g'(-1)\left(\sqrt{\xi_x^2+\xi_y^2}\right)^+Q^{com}_{f,l}=\\&\nabla Q^+_{f,l}\cdot\vec{n}-\nabla Q^-_{f,l}\cdot\vec{n}+S_f\sum_m\beta_{l,m}\frac{Q^-_{f,l}}{|V^-|}-g'(-1)Q^+_{f,l}\left(\sqrt{\xi_x^2+\xi_y^2}\right)^+\end{aligned} \tag{2.51}$$

Eq. (2.51) is also a linear system. The solved $Q^{com}_{f,l}$ are then put into (2.47) for ∇Q^{com}.

It may seem quite expensive to solve the linear system for each face, but the matrices are constant for fixed meshes, so they only need to be inverted once during the initialization. Therefore, the I-continuous approach can be made almost as efficient as the BR2 approach.

III. Numerical Tests

3.1 Couette Flow – Accuracy Test

Compressible Couette flow between two parallel walls is used to evaluate the accuracy of the method on irregular mixed grids. The computational domain is a 4X2 rectangular.

The exact solution for this case is

$$\begin{aligned}&u=\frac{U}{H}y,\ \ v=0\\&p=Const,\ \ \rho=\frac{p}{RT}\\&T=T_0+\frac{y}{H}(T_1-T_0)+\frac{\mu U^2}{2k}\frac{y}{H}\left(1-\frac{y}{H}\right)\end{aligned}\ . \tag{3.1}$$

The following parameters are chosen: the speed of the upper wall $U=0.3$, the temperature of the lower wall $T_0=0.8$, the temperature of the upper wall $T_1=0.85$, viscosity $\mu=0.01$, domain size in y direction $H=2$.

The LCP scheme is used for triangular elements while the FR scheme is used for quadrilateral elements. Both BR2 and I-continuous methods are tested for accuracy. The flow variables at boundary faces are simply fixed to the exact solution. All the tests cases presented below are obtained with a LUSGS implicit time integration approach [24], and all cases converge to machine zero. Density errors are used for the accuracy evaluation.

First, three meshes shown in Figure 4 are used for a mesh refinement study for 2^{nd} -- 4^{th} order schemes. The meshes are generated independently, rather in an h-refinement manner. The order of accuracy is calculated by

$$p = \frac{\ln\left(Er_1 / Er_2\right)}{\ln\left(\sqrt{N_2 / N_1}\right)} \tag{3.2}$$

where Er_1 and Er_2 are the error norms from Mesh 1 and Mesh 2, and N_1 and N_2 are the numbers of cells of Mesh 1 and Mesh 2.

The results for the BR2 and I-continuous approaches are shown in Table 1 and Table 2 respectively. There is no significant difference either in the error magnitude or in the order of accuracy. The BR2 approach performs better for the 3rd order cases while the I-continuous approach slightly outperforms BR2 for the 4th order cases. Although the achieved order of accuracy is slightly less than the optimal, one should note that these results are achieved with highly irregular and mixed meshes of poor quality.

Then, a p-refinement study is performed on a 10X5 mesh (Figure 4a), from k = 1 to 5. Figure 5 shows the convergence of both the BR2 and I-continuous approaches in L_2 norm. The two approaches show almost no difference in terms of accuracy.

3.2 Laminar Flow around a NACA0012 Airfoil

Viscous laminar flow around an NACA 0012 airfoil is then simulated with the LCP method, using both the BR2 and I-continuous approaches for viscous terms. 2nd, 3rd, and 4th order schemes are tested. The flow conditions are Mach = 0.5 and Re = 5000, with an angle of attack of 1 degree. Under such conditions, steady laminar separations are expected for both upper and lower surfaces of the airfoil.

Adiabatic no-slip wall condition is prescribed at the airfoil surface, and subsonic characteristic far field condition is used at the outer surface of the computational domain. The curve boundary is represented by piecewise cubic polynomials.

The computational domain extends 20 chord lengths away from the center of the airfoil. The mesh of 2692 cells, as is shown in Figure 6, is composed of regular quadrilateral elements near the airfoil and irregular mixed elements elsewhere, with some refinement at the trailing edge. A LUSGS solver is used for time integration and all cases are converged to machine zero.

The computed Mach number contours of 2nd – 4th order schemes are shown in Figure 7(a-c). Only the BR2 results are shown, since the I-continuous results are very similar. Due to the coarse mesh, the 2nd order results are not so smooth, especially at the wake. Note that for the 3rd and 4th order cases, the contour lines are smooth across the interfaces between regular cells and irregular ones, and also between triangular cells and quadrilateral ones. Visually, 3rd and 4th order results are very close to each other.

The skin friction coefficient C_f is defined as

$$C_f = \frac{\tau_w}{\frac{1}{2}\rho U_\infty^2} \tag{3.3}$$

where the shear stress at wall is computed by $|\tau_w| = \mu \frac{\partial V}{\partial n}$, with its sign chosen to be the same as $\frac{\partial u}{\partial n}$.

The C_f distribution near the separation point is shown in Figure 8. The 3rd and 4th order results are very close, showing a convergence of the p-refinement study. Besides, BR2 and I-continuous yield almost identical results for 3rd and 4th order cases.

The computed pressure drag coefficients $C_{D,p}$, friction drag coefficients $C_{D,f}$, and the separation points on the upper wall are shown in Table 3. All the data converges as the polynomial degree increases, and again, there is no significant difference between BR2 and I-continuous.

In order to estimate the efficiency of the BR2 and I-continuous approaches, the convergence history of the 4th order case is shown in Figure 9 (a,b). The same time step is used for both approaches, which is also the largest allowed. It can be seen that BR2 was able to converge with less iterations and CPU time for this case. Note that it takes 2,555 seconds to complete 3,000 iterations for BR2, and 2,654 seconds for I-continuous, showing the fact that the computational cost per one iteration of the two approaches is almost the same.

3.3 Unsteady Flow around a Circular Cylinder

The unsteady laminar flow around a cylinder is simulated with the LCP method, with 2^{nd} – 4^{th} order BR2 approach. The Reynolds number *Re = 75*, and the free stream Mach number *M = 0.2*. A vortex street is expected to form in the wake of the cylinder. The frequency of the vortex shedding is often denoted by the Strouhal number, defined by

$$St = \frac{f_s L_c}{U_\infty}. \tag{3.4}$$

The length scale L_c here is just the diameter of the cylinder. In an experimental study by Williamson [25], *St* was found to be 0.148.

The spatial discretization is the same: LCP for triangular elements and FR for quadrilateral elements. Subsonic far field boundary condition is used at the outer boundary of the domain, and adiabatic wall condition is used for the cylinder surface. A 2^{nd} order unsteady LUSGS solver is used for time integration.

The mesh is shown in Figure 10. It contains 2,028 cells, with regular quadrilateral cells near the cylinder and in the wake region, and irregular mixed cells elsewhere. The effects of domain size, time step and convergence criteria of inner iterations are carefully studied, in order to make sure the true numerical solution is approached.

The instantaneous Mach number contours are shown in Figure 11 (a-c). 2^{nd} order contours are not smooth, due to the relatively low resolution away from the cylinder. 3^{rd} and 4^{th} order results are similar, with 4^{th} order contours obviously smoother at 20 diameters downstream.

Table 3 shows the average drag coefficient $\overline{C_D}$ and computed *St* for *p=1-3*. Both converge as *p* increases, and the computed *St* is within the error range of known experimental data.

IV. Conclusions

The LCP method is extended to 2D Navier-Stokes equations on mixed meshes, with up to 6^{th} order accuracy. Two approaches are adopted in the LCP formulation for the discretization of the viscous flux, including the BR2 and recently proposed I-continuous approaches. This is the first attempt to extend the I-continuous approach for unstructured 2D simulations, and it is shown that it is an accurate and efficient approach for the 2D Navier-Stokes equations. Several test cases are presented for both steady and unsteady laminar flows, and BR2 and I-continuous show no significant difference in accuracy, efficiency or robustness. Future studies include the extension to 3D Navier-Stokes equations as well as the use of a p-multigrid technique for convergence acceleration.

Acknowledgments

The study was funded by AFOSR grant FA9550-06-1-0146, and partially by DOE grant DE-FG02-05ER25677. The views and conclusions contained herein are those of the authors and should not be interpreted as necessarily representing the official policies or endorsements, either expressed or implied, of AFOSR, DOE, or the U.S. Government.

References

[1]B. Cockburn and C.-W. Shu, TVB Runge-Kutta local projection discontinuous Galerkin finite element method for conservation laws II: general framework, Mathematics of Computation 52, 411-435 (1989).

[2]B. Cockburn, S.-Y. Lin and C.-W. Shu, TVB Runge-Kutta local projection discontinuous Galerkin finite element method for conservation laws III: one-dimensional systems, J. Comput. Phys. 84, 90-113 (1989).

[3]B. Cockburn and C.-W. Shu, The Runge-Kutta discontinuous Garlerkin method for conservation laws V: multidimensional systems, J. Comput. Phys., 141, 199 - 224, (1998).

[4]F. Bassi and S. Rebay, High-order accurate discontinuous finite element solution of the 2D Euler equations, J. Comput. Phys. 138, 251-285 (1997).

[5]F. Bassi and S. Rebay, A high-order accurate discontinuous finite element method for the numerical solution of the compressible Navier–Stokes equations. J Comp Phys 1997;131(1):267–79.

[6]Z.J. Wang, Spectral (Finite) volume method for conservation laws on unstructured grids: basic formulation, J. Comput. Phys. Vol. 178, pp. 210-251, 2002.

[7]Z.J. Wang, High-order methods for the Euler and Navier-Stokes equations on unstructured grids, Journal of Progress in Aerospace Sciences, Vol. 43, pp. 1-47, 2007.

[8]Z.J. Wang, and Y. Liu, Spectral (finite) volume method for conservation laws on unstructured grids ii: extension to two-dimensional scalar equation, J. Computational Physics, Vol. 179, pp. 665-697, 2002.

[9]Z.J. Wang and Y. Liu, Spectral (finite) volume method for conservation laws on unstructured grids iii: one-dimensional systems and partition optimization, Journal of Scientific Computing, Vol. 20, No. 1, pp. 137-157 (2004).
[10]Z.J. Wang, L. Zhang and Y. Liu, Spectral (Finite) Volume Method for Conservation Laws on Unstructured Grids IV: Extension to Two-Dimensional Euler Equations, Journal of Computational Physics Vol. 194, No. 2, pp. 716-741 (2004).
[11]Y. Liu, Vinokur M, and Wang ZJ. "Discontinuous Spectral Difference Method for Conservation Laws on Unstructured Grids," in Proceedings of the 3rd International Conference on Computational Fluid Dynamics, Toronto, Canada, July 12-16 2004.
[12]Y. Liu, Vinokur M, and Wang ZJ. "Discontinuous Spectral Difference Method for Conservation Laws on Unstructured Grids," Journal of Computational Physics Vol. 216, pp. 780-801 (2006).
[13]G. May and A. Jameson, "A spectral difference method for the Euler and Navier-Stokes equations", AIAA paper No. 2006-304, 2006.
[14]H.T. Huynh, A flux reconstruction approach to high-order schemes including discontinuous Galerkin methods, AIAA Paper 2007-4079.
[15]Z.J.Wang and H. Gao, A Unifying Lifting Collocation Penalty Formulation for the Euler Equations on Mixed Grids, AIAA Paper 2009-0401.
[16]F.Bassi and S. Rebay, GMRES Discontinuous Galerkin Solution of the Compressible Navier-Stokes Equations. In Karniadakis Cockburn and Shu, editors, 208. Springer, Berlin, 2000.
[17]B. Cockburn and C.-W. Shu, The local discontinuous Galerkin methods for time-dependent convection diffusion systems, SIAM J. Numer. Anal., 35(1998), pp. 2440-2463.
[18]J. Peraire and P.-O. Persson, The compact discontinuous Galerkin (CDG) method for elliptic problems, SIAM J. Sci. Comput., Vol. 30, No. 4 (2008) pp. 1806-1824
[19]B. van Leer and S. Nomura, Discontinuous Galerkin for Diffusion, AIAA Paper 2005-5108.
[20]H. T. Huynh, A Reconstruction Approach to High-Order Schemes Including Discontinuous Galerkin for Diffusion, AIAA Paper 2009-403.
[21]C. Liang, A. Jameson and Z. J. Wang, "Spectral Difference method for two-dimensional compressible flow on unstructured grids with mixed elements", Journal of Computational Physics, vol 228, pp 2847-2858, 2009.
[22]D.A. Kopriva and J.H. Kolias, A conservative staggered-grid Chebyshev multidomain method for compressible flows, J. Comp. Physics, 125(1996), pp. 244-261.
[23]P.L. Roe, Approximate Riemann solvers, parameter vectors, and difference schemes, J. Comput. Phys. 43 357-372 (1981).
[24]Y. Sun, Z.J. Wang, and Y. Liu, Efficient implicit non-linear LU-SGS approach for compressible flow computation using high-order spectral difference method, Commun. Comput. Phys. Vol. 5, No. 2-4, pp. 760-778.
[25]C. H. K. Williamson. Oblique and parallel modes of vortex shedding in the wake of a cylinder at low Reynolds number, J. Fluid Mech., 206:579–627, 1989.

Table 1 Couette Flow Accuracy Results with BR2

Polynomial Degree	Grid Size	L_1 error	L_1 order	L_2 error	L_2 order	L_∞ error	L_∞ order
1	10X5	5.731e-05	-	7.261e-05	-	2.425e-04	-
	20X10	1.799e-05	1.64	2.312e-05	1.62	1.145e-04	1.06
	40X20	5.490e-06	1.82	7.151e-06	1.80	3.506e-05	1.82
2	10X5	6.320e-07	-	8.914e-07	-	5.023e-06	-
	20X10	9.545e-08	2.68	1.309e-07	2.72	6.873e-07	2.82
	40X20	1.535e-08	2.81	2.091e-08	2.82	1.145e-07	2.75
3	10X5	6.258e-09	-	8.525e-09	-	6.986e-08	-
	20X10	4.807e-10	3.64	6.525e-10	3.64	4.965e-09	3.75
	40X20	4.054e-11	3.80	5.785e-11	3.72	4.505e-10	3.69

Table 2 Couette Flow Accuracy Results with I-continuous

Polynomial Degree	Grid Size	L_1 error	L_1 order	L_2 error	L_2 order	L_∞ error	L_∞ order
1	10X5	5.065e-05	-	7.112e-05	-	2.677e-04	-
	20X10	1.796e-05	1.47	2.306e-05	1.60	1.062e-04	1.31
	40X20	5.497e-06	1.82	7.162e-06	1.80	3.991e-05	1.50
2	10X5	6.301e-07	-	8.795e-07	-	4.877e-06	-
	20X10	1.029e-07	2.57	1.400e-07	2.61	8.697e-07	2.44
	40X20	1.852e-08	2.63	2.456e-09	2.67	1.568e-07	2.63
3	10X5	6.100e-09	-	8.190e-09	-	7.536e-08	-
	20X10	4.616e-10	3.66	6.157e-10	3.67	4.843e-09	3.89
	40X20	3.698e-11	3.88	5.186e-11	3.80	4.235e-10	3.74

Table 3 P-refinement study of the flow around NACA 0012 airfoil

Viscous Discretization -- Polynomial Degree	$C_{D,p}$	$C_{D,f}$	Separation Point (Upper Wall)
BR2--1	0.02516	0.03230	80.43%
I-Continuous--1	0.02497	0.03271	79.01%
BR2--2	0.02251	0.03274	69.17%
I-Continuous--2	0.02247	0.03275	69.15%
BR2--3	0.02274	0.03253	68.35%
I-Continuous--3	0.02273	0.03252	68.31%
BR2--5	0.02269	0.03248	68.25%
I-Continuous--5	0.02269	0.03248	68.25%

Table 4 P-refinement study for unsteady flow around a cylinder

Viscous Method -- Polynomial Degree	$\overline{C_D}$	St
BR2--1	1.053	0.153
BR2--2	1.037	0.153
BR2--3	1.035	0.153

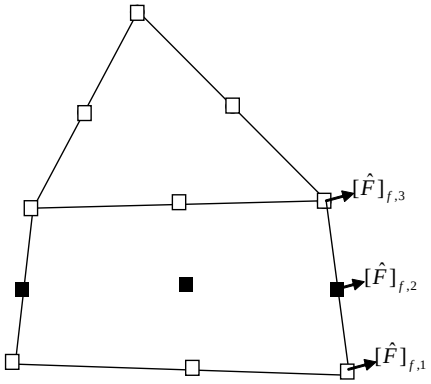

Figure 1. Solution points for the 3rd order LCP scheme on hybrid meshes

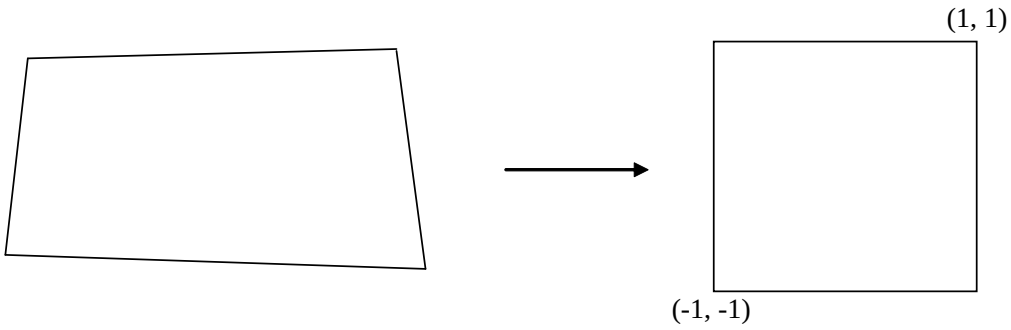

Figure 2. Transformation of a quadrilateral element to a standard element

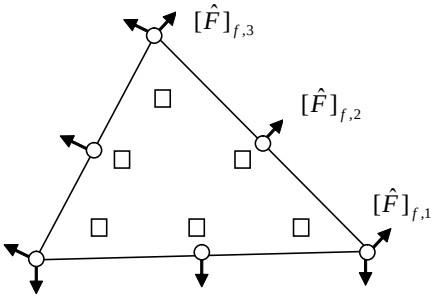

Figure 3. Solution points (squares) and flux points (circles) for k = 2

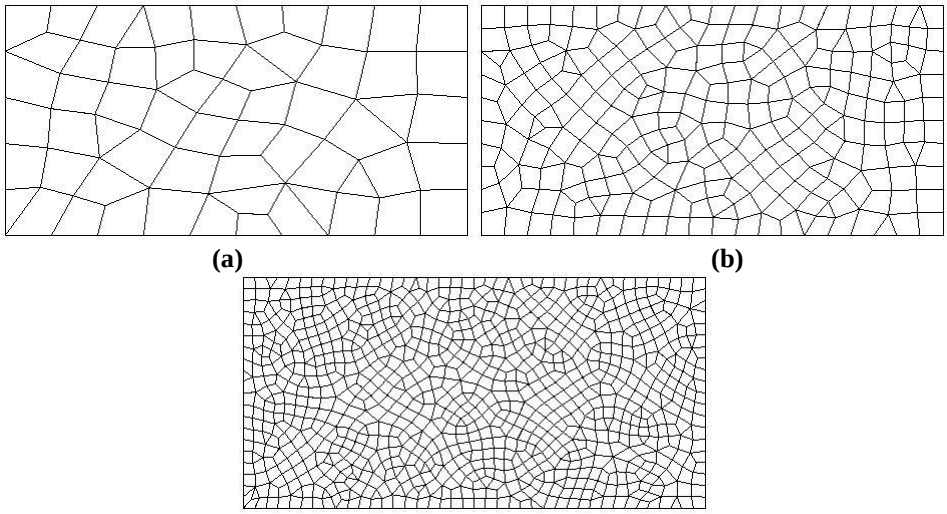

(a) **(b)**

(c)

Figure 4. Mixed mesh used for Couette flow (a) 10X5 with 61 cells (b) 20X10 with 250 cells (c) 40X20 with 919 cells

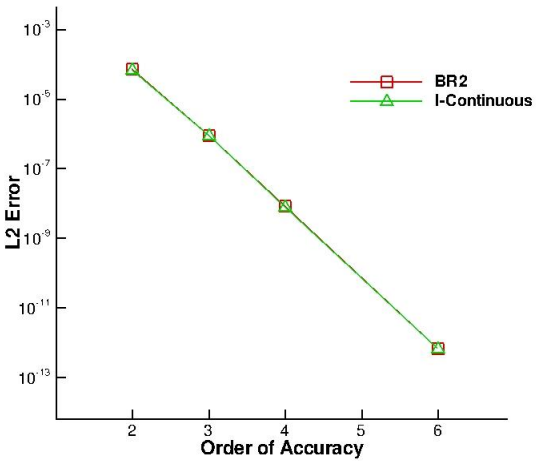

Figure 5. P-refinement study for Couette flow with a 10X5 mesh

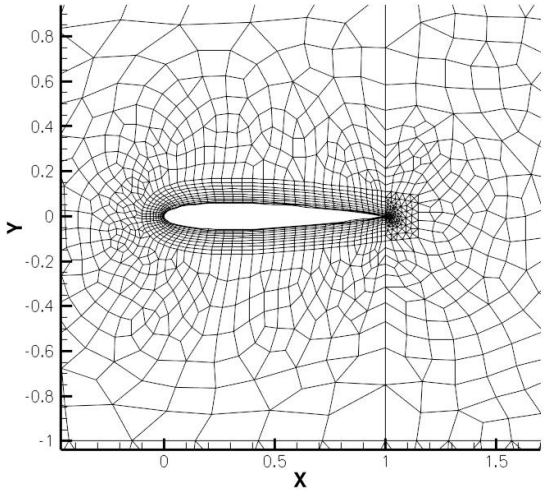

Figure 6. Mixed mesh around an NACA0012 airfoil

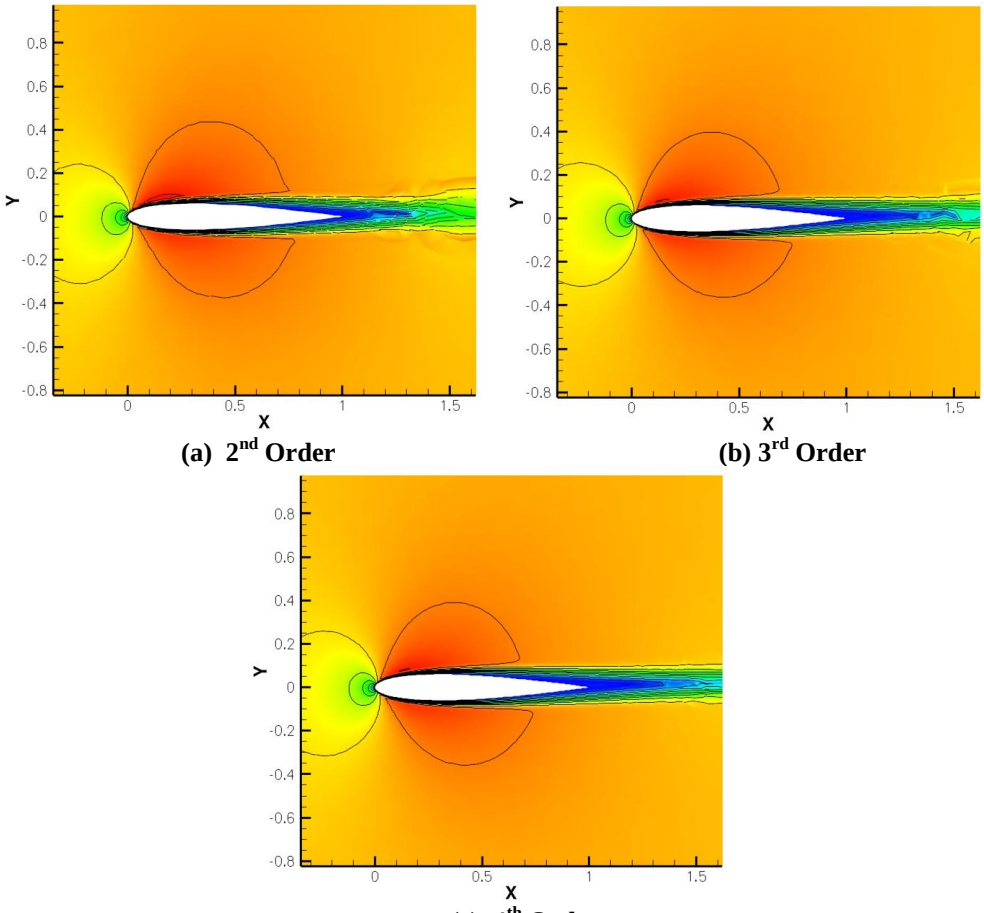

(a) 2nd Order **(b) 3rd Order**

(c) 4th Order

Figure 7. Mach number contours of flow around an NACA 0012 airfoil

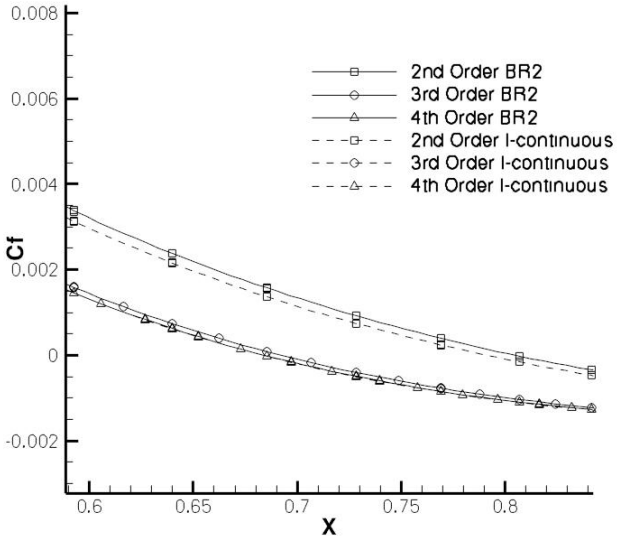

Figure 8. C_f distributions on upper wall near the separation point

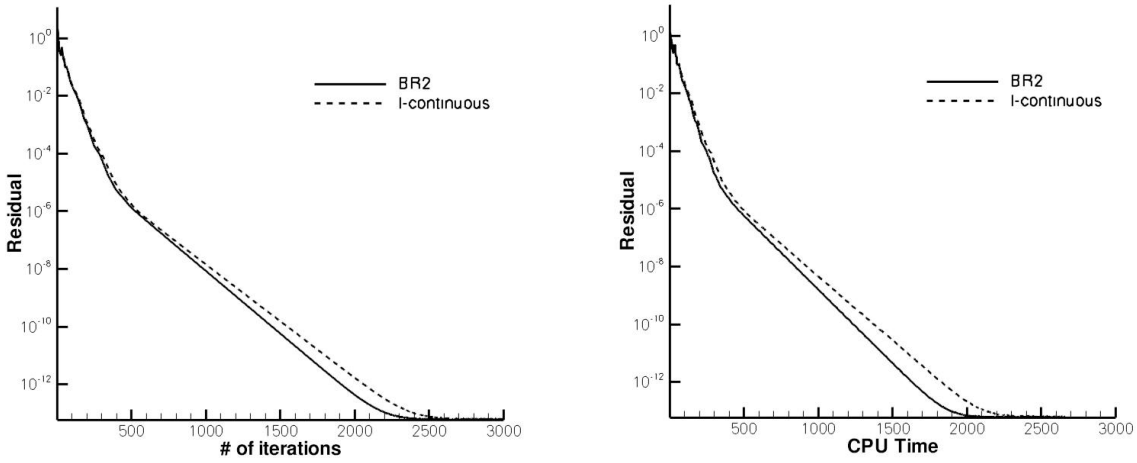

(a) **(b)**

Figure 9. Convergence history for flow around NACA 0012 airfoil

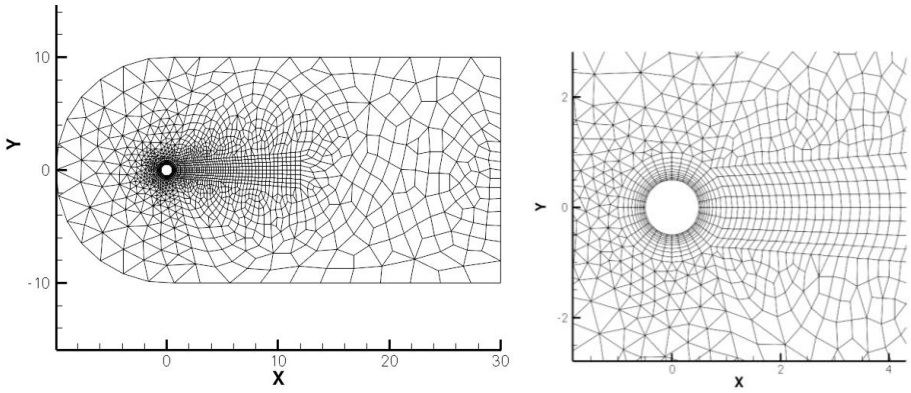

(a) The whole domain **(b) near the cylinder**

Figure 10. Mixed mesh for unsteady flow around a cylinder

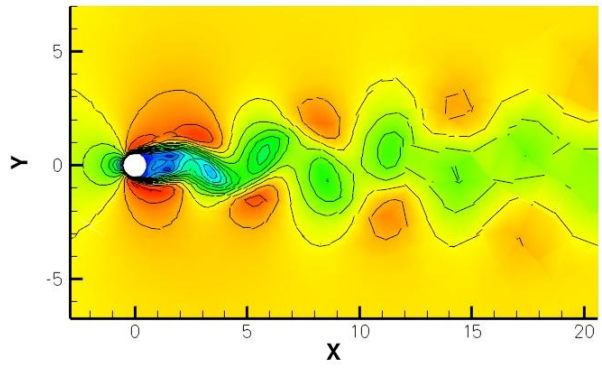

(a) 2nd order

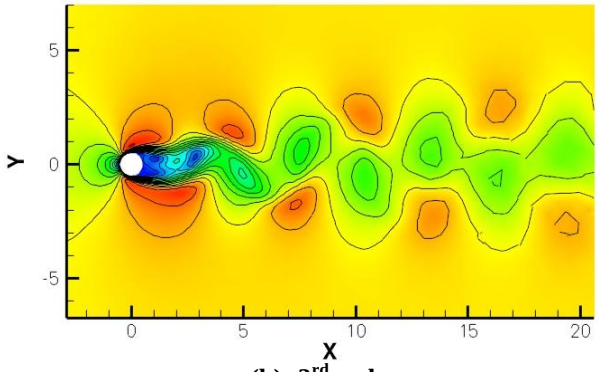

(b) 3rd order

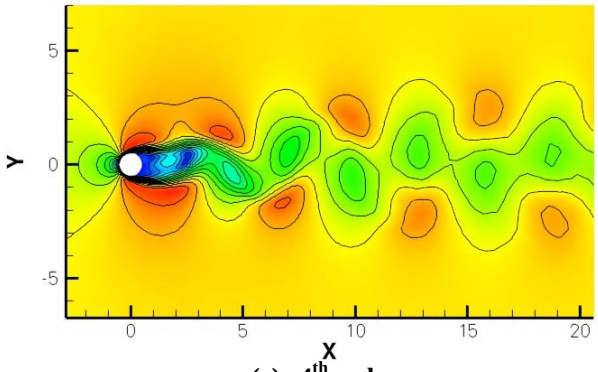

(c) 4th order

Figure 11. Mach number contours for unsteady flow around a cylinder